# Amyloid-Derived Peptide Forms Self-Assembled Monolayers on Gold Nanoparticle with a Curvature-Dependent $\beta$-Sheet Structure

**Christopher P. Shaw,[†] David A. Middleton,[†] Martin Volk,[‡,*] and Raphaël Lévy[†,*]**

[†]Institute of Integrative Biology, University of Liverpool, Liverpool L69 7ZB, United Kingdom and [‡]Department of Chemistry and Surface Science Research Centre, University of Liverpool, Liverpool L69 3BX, United Kingdom

**ABSTRACT**

Using a combination of Fourier transform infrared (FTIR) spectroscopy and solid-state nuclear magnetic resonance (SSNMR) techniques, the secondary structure of peptides anchored on gold nanoparticles of different sizes is investigated. The structure of the well-studied CALNN-capped nanoparticles is compared to the structure of nanoparticles capped with a new cysteine-terminated peptide, CFGAILSS. The design of that peptide is derived from the minimal amyloidogenic sequence FGAIL of the human islet polypeptide amylin. We demonstrate that CFGAILSS forms extended fibrils in solution. When constrained at a nanoparticle surface, CFGAILSS adopts a secondary structure markedly different from CALNN. Taking into account the surface selection rules, the FTIR spectra of CFGAILSS-capped gold nanoparticles indicate the formation of $\beta$-sheets which are more prominent for 25 nm diameter nanoparticles than for 5 nm nanoparticles. No intermolecular $^{13}C-^{13}C$ dipolar coupling is detected with rotational resonance SSNMR for CALNN-capped nanoparticles, while CALNN is in a random coil configuration. Coupling is detected for CFGAILSS-capped gold nanoparticles, however, consistent with an intermolecular $^{13}C-^{13}C$ distance of 5.0 $\pm$ 0.3 Å, in agreement with intermolecular hydrogen bonding in a parallel $\beta$-sheet structure.

**KEYWORDS:** amyloid · self-assembly · FTIR · solid-state NMR · biomimetic · peptide-capped nanoparticles

In the past two decades, a range of water-soluble multifunctional nanomaterials composed of an inorganic core surrounded by a small molecule capping layer have been prepared and, in some instances, described as protein-like. Proteins are both a benchmark and a source of inspiration for the design of those materials, which, ideally, will combine the distinct physical properties of inorganic nanoparticles with the remarkable (bio)chemical properties of proteins. Major differences remain, however, between proteins and these synthetic analogues. Proteins are nanoscale objects where the exact position of each residue, often critical to their function, is obtained through the use of template mRNA for the primary structure followed by noncovalent interactions, self-assembly, and self-organization leading to the secondary, tertiary, and quaternary structure. In contrast, the small molecules forming the organic capping layer of core–shell nanomaterials obtained to date tend to have an uncontrolled and often unknown structure at the molecular level.

Gold nanoparticles are an attractive model system because of the well-developed particle syntheses, ease of surface functionalization (Au-thiol chemistry), and possibility of monolayer reorganization through ligand diffusion[1,2] and ligand exchange.[3] Previous efforts have focused on both the structural characterization and the design of synthesis routes leading to controlled complex ligand shells. A major step has been the recent elucidation of the structure of thiolates on $Au_{102}$, which has revealed chirality, unexpected geometries, and provided details of the Au–S bond geometry, reinforcing the analogy between these clusters and proteins.[4] Other recent developments toward a better characterization of the nanoparticle capping layers include electron paramagnetic resonance studies,[3] electron microscopy showing individual ligands using polyoxometalate complexes,[5] chemical cross-linking,[6] as well as scanning tunneling microscopy,[7] although the latter is prone to artifacts and the interpretation is controversial.[8] Several strategies have been tested to force the self-organization in mixtures of ligands, from nonconstrained self-organization of multiple ligands[6,9] to

* Address correspondence to m.volk@liverpool.ac.uk, rapha@liverpool.ac.uk.

Received for review November 1, 2011 and accepted January 13, 2012.

**Published online January 13, 2012**
10.1021/nn204214x

"templating" using soluble target molecules,[10] and engineering of patches using adsorption of nanoparticles on surfaces as a "mask" for selective functionalization.[11]

In 2004, we reported the rational and combinatorial design of peptides that bind to gold nanoparticles using the cysteine thiol side chain and form dense self-assembled monolayers (SAMs), increasing colloidal stability and providing a versatile means of functionalization.[12] In that initial study, hydrophobic interactions between adjacent peptides were used to drive a high surface coverage, leading to a compact SAM, for example, with the peptide CALNN, and the combinatorial study provided insights into intermolecular interactions, but the secondary structure of the peptide monolayer remained unknown. Using IR and $^1$H NMR, Maran *et al.* reported the presence of hydrogen bonding in conformationally constrained peptide layers (based on α-aminoisobutyric acid units) on 1−2 nm gold nanoparticles.[13] Rio-Echevarria *et al.* have reported the capping of particles of a similar size with helix-structured undecapeptide using $C^{\alpha}$-tetrasubstituted α-amino acids,[14] and a hypothetical $\beta$-type structure has been proposed by Olmedo *et al.* for the peptide CLPFFD-$NH_2$ on 12.5 nm gold nanoparticles.[15] In the latter studies, circular dichroism was used as the structural characterization technique, indicating that this technique can provide qualitative insights for small particles in spite of the strong absorbance of gold nanoparticles in the UV. Similarly, IR spectroscopy, which also is highly sensitive to the secondary structure of peptides, has been used,[13] although the interpretation of IR spectra must account for the so-called surface selection rules (*vide infra*), which also apply on the surface of metal nanoparticles[16] but have been largely overlooked in the literature.[17] The development of peptide-capped nanomaterials has been expanding in recent years with a number of other peptides being proposed as gold nanoparticle capping agents or as dual reducing and capping agents.[18−21]

The present work builds on structural biology investigation principles and tools to design and characterize thin peptide layers on gold nanoparticles which have different secondary structure motifs and supramolecular organization. A number of short peptides can assemble into amyloid-like fibrils where intermolecular hydrogen bonds lead to the characteristic cross-$\beta$ structure that is the hallmark of larger protein fibrils associated with amyloid disease.[22,23] Because of the specific intermolecular directional assembly, we envisioned that such peptides could constitute a new category of building blocks to engineer complex nanoparticles. We introduce a new peptide, CFGAILSS, which is based on the minimal amyloidogenic sequence FGAIL of the human islet polypeptide amylin.

The incorporation of the sulfhydryl group enables derivatization of the gold nanoparticles, and the native diserine motif of amylin is preserved in order to present a hydrophilic surface to the aqueous environment. Modifications to the FGAIL template are well-known to result in fibrillar aggregates with different morphologies and molecular architectures. For example, FGAIL and NFGAIL assemble into completely different fibrillar assemblies,[24] and SNNFGAILSS has been shown to associate into both antiparallel and parallel $\beta$-sheets.[25] Thus, it was not known at the outset of this work whether CFGAILSS forms fibrillar aggregates or indeed whether it spontaneously self-assembles at all.

Using Fourier transform infrared (FTIR) spectroscopy in aqueous solution and solid-state NMR, we elucidate the structure of both CALNN and CFGAILSS in solution and on spherical gold particles of diameters from 5 to 25 nm and demonstrate that CALNN exhibits a random coil configuration in all cases, whereas CFGAILSS adopts a curvature-dependent conformation toward parallel $\beta$-sheet with a significant proportion of intermolecular hydrogen bonding.

## RESULTS AND DISCUSSION

**Peptide Self-Assembly in Solution.** To evaluate if the addition of a cysteine to the FGAILSS motif preserved the amyloid forming properties, the assembly of the peptide CFGAILSS in aqueous solution was investigated. When lyophilized CFGAILSS is dissolved into water or phosphate buffer saline at mg/mL concentration, visual observation reveals the rapid formation of aggregates (cloudiness).

The amide I′ band (the prime indicating deuterated amides) of the FTIR spectrum is highly sensitive to the secondary structure of the peptide.[26] The solution FTIR spectrum of CFGAILSS exhibits two amide I′ bands at 1689 and 1624 $cm^{-1}$, the former being much smaller than the latter (Figure 1A), which is indicative of an antiparallel $\beta$-sheet structure.[27,28] The modified peptide CFGAILSS, like its parent peptide NNFGAILSS, forms extended fibrils in solution, as shown by transmission electron microscopy (Figure 1B). Figure 1C shows a $^{13}$C CP-MAS NMR spectrum of fibrils produced from a 1:1 mixture of [$^{13}$C′-A]CFGAILSS and [$^{13}$Cα-A]CFGAILSS. Peaks at 171.6 and 47.3 ppm correspond to C′ and Cα, respectively. Chemical shift and line widths for the fibrils and all peptide samples described subsequently are summarized in Table 1. The relatively narrow line widths and single peaks for the fibrils are consistent with a reasonable degree of long-range order as expected for an extended array of hydrogen-bonded peptides. Altogether, these results demonstrate that CFGAILSS forms ordered, homogeneous fibrils with an antiparallel $\beta$-sheet conformation. CALNN, on the other hand, has an amide I′ band at 1648 $cm^{-1}$, indicative of the random coil structure,[26,29,30] and shows no visible aggregation at mg/mL concentration of fibrils in TEM.

Having obtained two cysteine-terminated peptides, CALNN and CFGAILSS, which have different self-assembly

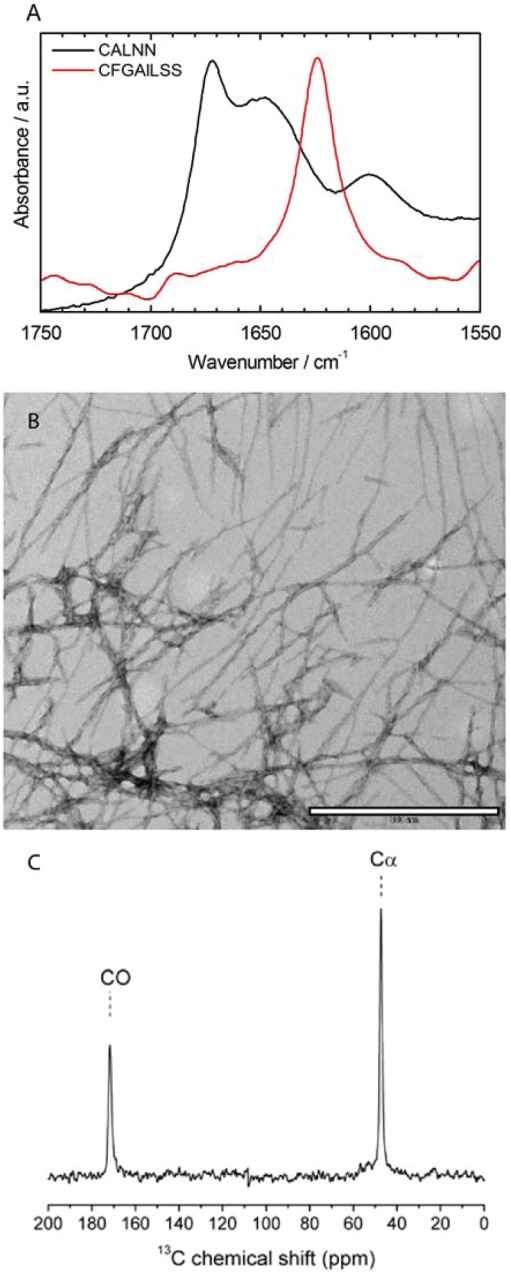


**Figure 1. Solution assembly of CALNN and CFGAILSS. (A) FTIR spectra of CALNN (black) and CFGAILSS (red); the sharp band at 1672 $cm^{-1}$ in the CALNN sample did contain trifluoroacetate ions (TFA) from the synthesis process, which give rise to (B) electron microscopy with negative staining of CFGAILSS fibrils (no fibrils observed with CALNN); (C) $^{13}C$ CP-MAS NMR spectrum of 1:1 [$^{13}C'$-A]CFGAILSS/[$^{13}C\alpha$-A]CFGAILSS fibrils.**

properties and molecular structure in solution, we then evaluated their respective structure and molecular organization when they are constrained at the surface of nanoparticles of different sizes.

**Considerations on Nanoparticle Synthesis.** To test the effect of surface curvature on molecular structure, gold cores of 5, 8, 10, and 25 nm diameters were prepared by aqueous reduction of $HAuCl_4$ (Supporting Information, Figure S1). The classical citrate route was considered initially but eventually deemed unsuitable because of the large absorbance of citrate carboxyls at 1580 $cm^{-1}$, which distorts the FTIR spectrum in the amide I′ band region (it appears that the peptide monolayer does not entirely displace the citrate when tannic acid is used as a co-reducing agent).[31] Since acrylate has only one carboxyl group, compared to the three carboxyls of citrate, a combination of sodium acrylate and tannic acid was used as reducing agents/weakly adsorbed capping ligands for the synthesis of the 5, 8, and 10 nm cores. In the case of the seeded growth (25 nm diameter nanoparticles), a minimum amount of citrate is required for the synthesis.

**TABLE 1. Summary of $^{13}C$ Chemical Shifts and Line Widths at Half-Height for C′ and Cα of CFGAILSS Fibrils and CFGAILSS- and CALNN-Capped Nanoparticles**

| | chemical shift (ppm) | | line width (Hz) | |
|---|---|---|---|---|
| sample | C′ | Cα | C′ | Cα |
| CFGAILSS fibrils | 171.6 | 47.3 | 125.2 | 115.1 |
| CFGAILSS nanoparticle | | | | |
| 5 nm | 170.8 | 46.4 | 300.0 | 307.9 |
| 10 nm | 171.3 | 47.0 | 415.5 | 588.6 |
| CALNN nanoparticle | | | | |
| 5 nm | 172.6 | 48.7 | 473.0 | 435.6 |
| 10 nm | 171.8 | 48.6 | 452.4 | 450.6 |

**Formation of the Peptide SAM on Nanoparticles.** We have previously reported a simple route to obtain peptide-capped gold nanoparticles in a one-step procedure, that is, mixing the aqueous colloidal suspension with an aqueous solution of the thiolated peptide.[6,32−34] This procedure was followed here to prepare the CALNN-capped nanoparticles but had to be adapted for CFGAILSS since the peptide aggregates were dispersed in, or diluted in, an aqueous buffer. Hexafluoro-2-propanol (HFIP) exhibits strong hydrogen bonding properties and has been reported to be a good solvent for amyloid peptides leading to the dissolution of amyloid proto structures and fibrils.[35] Dissolution of lyophilized CFGAILSS into HFIP provides indeed a clear solution even at concentrations above 10 mM. When an HFIP solution of CFGAILSS peptide is added to the aqueous colloidal suspension, two processes occur in parallel: the formation of amyloid fibers and the reaction between the cysteine and the gold leading to the formation of the peptide monolayer on the nanoparticle surface. In order to obtain nanoparticles capped with a dense layer of CFGAILSS, a protocol was developed to force the assembly on the nanoparticle surface of this peptide that will otherwise self-assemble into fibrils (see Supporting Information for details). Briefly, following the first overnight incubation with peptide, the nanoparticle−fibril supramolecular networks (Figure 2A) were dried using a rotary evaporator; HFIP was then added, and the particles were sonicated and

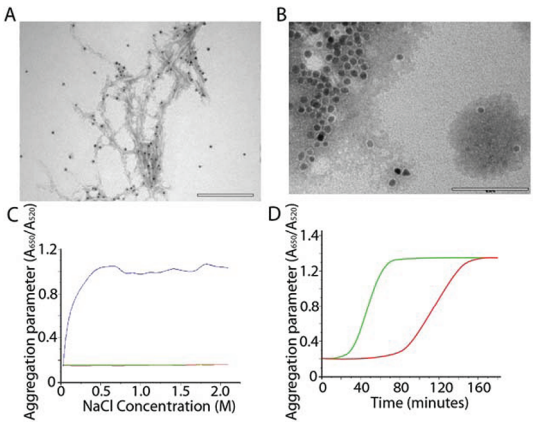


**Figure 2. CFGAILSS, from fibrils to SAMs; (A) TEM of fibril–nanoparticle (8 nm) assemblies formed during the first step of the capping process; (B) TEM after completion of the capping process and removal of the excess peptide; (C) stability against salt-induced aggregation of 10 nm diameter CALNN-capped (green), CFGAILSS-capped (red), and citrate-capped (blue) nanoparticles; (D) stability against DTT ligand exchange, salt-induced aggregation of 10 nm diameter CALNN-capped (green), and CFGAILSS-capped (red) nanoparticles in the presence of 100 mM DTT. In image (A), the scale bar represents 500 nm, and in image (B), the scale bar represents 100 nm.**

left overnight. In HFIP, the fibrils were dissolved leading to additional free peptide that was available to react and complete the SAM on the particles. The particles precipitated slowly overnight. The particles were centrifuged at 5000*g* for 10 min, forming a very dense pellet, allowing most of the HFIP containing peptide to be removed. The particles were then resuspended in 0.2 M NaOH, and excess peptide and base was then removed by a Sephadex G25 size exclusion chromatography column, leading to CFGAILSS-capped gold nanoparticles that were colloidally very stable in aqueous solutions. Electron microscopy with negative staining confirmed the disappearance of the fibrils, and a white corona could be seen around the nanoparticles, suggesting the formation of the peptide layer (Figure 2B).

To confirm the formation of the monolayer, the extent of colloidal stabilization was measured. When exposed to increasing ionic strength, CFGAILSS-capped nanoparticles show a similar level of colloidal stability as CALNN (Figure 2C). Resistance of the monolayer to ligand exchange with small molecules is an indication of the compactness of the capping layer.[36] To compare the resistance of monolayers to ligand exchange by dithiothreitol (DTT), CALNN and CFGAILSS-capped 10 nm nanoparticles were treated with DTT. DTT is a small, uncharged molecule with two thiol groups. It readily exchanges with other ligands on the surfaces of gold nanoparticles. As it replaces the peptide monolayer, it also reduces the steric and electrostatic barrier that keeps the gold nanoparticles from aggregating. If ligand exchange is done at high ionic strength, it is possible to detect ligand exchange simply by monitoring the extent of aggregation by the red shift in the plasmon band. Aggregation of CFGAILSS-capped nanoparticles induced by ligand exchange with DTT is more than two times slower than for CALNN-capped nanoparticles, suggesting that CFGAILSS adopts a different structure in the SAM (Figure 2D).

The colloidal stability and resistance to ligand exchange confirm the formation of a compact CFGAILSS monolayer at the surface of the gold nanoparticles. These results also indicate that peptides attached to two different particles are unable to form antiparallel $\beta$-sheets by intercalation. The peptide grafting density of the CFGAILSS monolayer on gold nanoparticles was measured by amino acid analysis, indicating a coverage of 2.55 $\pm$ 0.14 peptides/nm$^2$ (Supporting Information), similar to CALNN (2.4 peptides/nm$^2$).[37] Given that in identical conditions the peptide CFGAILSS aggregates instantaneously into micrometer size fibrils, it is remarkable that CFGAILSS-capped nanoparticles have an extremely good colloidal stability. This is most likely due to charge repulsion between the terminal carboxylic acid as well as steric hindrance due to the compact peptide monolayers.

**Fourier Transform Infrared Spectroscopy Investigation of CALNN-Capped and CFGAILSS-Capped Nanoparticles.** FTIR spectroscopy is widely used for characterizing the secondary structure of proteins and peptides. Of particular interest in this context is the amide I′ band around 1650 cm$^{-1}$, which mainly involves the amide carbonyl stretch and has been shown to be highly sensitive to peptide secondary structure.[26,30] Gold nanoparticles are transparent in this region of the electromagnetic spectrum, so *in situ* measurements of SAMs on gold nanoparticles are possible. However, the interpretation of IR spectra of small molecules bound to metal nanoparticles requires some careful considerations of the so-called surface selection rules, which will be discussed in more detail below.

Figure 3 shows the FTIR spectra of CALNN- and CFGAILSS-capped gold nanoparticles. These spectra indicate clearly a difference of conformation between the CALNN and CFGAILSS capping layers, at least for the larger nanoparticles, and point toward a diameter-dependent conformation of the CFGAILSS SAMs.

Figure 3A compares the FTIR spectra of CALNN peptide in solution (black dotted line) and as a SAM on gold nanoparticles of 8 nm (magenta), 10 nm (blue), and 25 nm (green) diameter. As noted before, the solution sample did contain excess TFA ions, which give rise to the sharp band at 1672 cm$^{-1}$; these are removed in the various cleaning steps during SAM formation on gold nanoparticles. The band at 1600 cm$^{-1}$ arises from the carboxyl groups at the end of the peptide backbone (and possibly residual acrylate in the nanoparticle samples), whereas the main band at around 1650 cm$^{-1}$ is the amide I′ band. For the solution

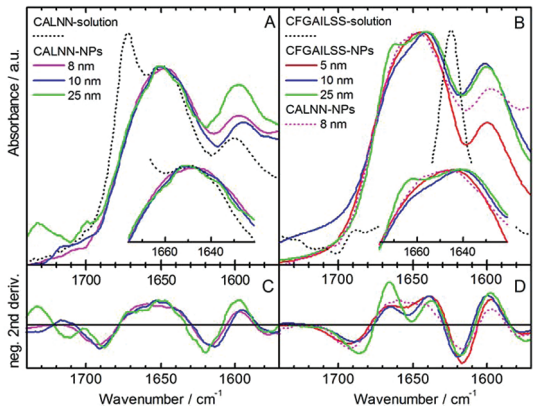


**Figure 3. FTIR spectra of (A) CALNN peptide in solution and CALNN-capped gold nanoparticles (8, 10, and 25 nm diameter) and (B) CFGAILSS peptide in solution and CFGAILSS-capped gold nanoparticles (5, 10, and 25 nm diameter). for comparison, the spectrum of CALNN-capped nanoparticles with 8 nm diameter is reproduced in (B); the insets in (A) and (B) show details of the spectra near the maximum of the amide I′ band. All spectra have been scaled to have the same maximum amide I′ absorbance. Panels (C) and (D) show the negative second derivative of the NP-FTIR spectra in (A) and (B), respectively.**

as well as for the nanoparticle samples, the amide I′ band consists of a broad unstructured peak with a maximum at ~1650 $cm^{-1}$, as expected for a disordered peptide.[26,29,30] This result is unsurprising, given the original design criteria, and is also in agreement with molecular dynamic simulations of a CALNN monolayer.[37] The identical shape of the amide I′ band for CALNN-capped nanoparticles of different size shows that there is no significant effect of the nanoparticle size on the secondary structure of the peptide capping layer. For a more detailed investigation, the second derivatives of the FTIR spectra were calculated, which is a widely used band-narrowing and deconvolution technique based on the fact that the negative second derivative of an individual band has a maximum at the same position as the original band, but with a smaller bandwidth, thus allowing the resolution of strongly overlapping individual bands.[26] Figure 3C shows that the second derivative spectra of CALNN-capped nanoparticles of different size are essentially identical and broad with a maximum at 1650 $cm^{-1}$, confirming the disordered nature of the capping layer for all nanoparticle sizes investigated here.

Figure 3B shows that the FTIR spectra of the CFGAILSS-capped nanoparticles are significantly different, indicating a nanoparticle-induced change in the structure of the peptide between its solution (fibril) and SAM configurations. For all CFGAILSS−nanoparticle samples, the absence of the dominant band at 1624 $cm^{-1}$ and the small band at 1689 $cm^{-1}$ indicates that there is no significant amount of antiparallel $\beta$-sheet fibrils present, as expected due to the geometrical constraint of the SAM, with CFGAILSS being anchored to the gold through the N-terminal cysteine which determines the orientation of the peptides within the SAM. The absence of the antiparallel $\beta$-sheet bands also confirms that no significant amount of free peptide remains in the sample. For nanoparticles with 5 nm diameter (red), the amide I′ band seems similar to that found for CALNN-capped nanoparticles (dotted magenta line), that is, a broad band centered at 1645−1650 $cm^{-1}$, suggesting the presence of some disordered peptide backbone. However, closer inspection of this band and the second derivative spectrum in Figure 3D hints at the presence of two separate, although strongly overlapping, bands at ~1640 and ~1665 $cm^{-1}$. It has to be noted that second derivative spectra emphasize the contributions from narrow bands over those of broader, unstructured bands; thus, it seems possible that the amide I′ band of 5 nm CFGAILSS-capped nanoparticles is dominated by a broad band at 1650 $cm^{-1}$ with a smaller contribution from the two narrower bands at 1640 and 1665 $cm^{-1}$. The existence of these two bands becomes much clearer in the FTIR spectrum of CFGAILSS-capped gold nanoparticles of 10 nm diameter (blue), which has a maximum at ~1640 $cm^{-1}$ with a pronounced shoulder at ~1665 $cm^{-1}$, yielding two separate peaks in the second derivative spectrum. For CFGAILSS-capped nanoparticles with 25 nm diameter (green), the two bands are resolved even in the FTIR spectrum (Figure 3B). These narrow amide I′ bands show that for CFGAILSS-capped nanoparticles the capping layer adopts a more ordered structure and that the extent of ordering increases with increasing nanoparticle size.

As discussed above, the CFGAILSS capping peptide was designed based on the high propensity of the NNFGAILSS sequence for forming $\beta$-sheets. Since the N-terminus of the capping peptide is bound to the gold nanoparticle surface, only parallel $\beta$-sheet formation is possible in the capping layer. Similar to the antiparallel $\beta$-sheet structure, the parallel $\beta$-sheet conformation is characterized by two narrow amide I′ bands, although these two bands are not as well separated as for antiparallel $\beta$-sheets, with a dominant band at slightly higher frequencies than those found for antiparallel $\beta$-sheets (*i.e.*, ~1630 $cm^{-1}$), and a much weaker band which is split from this band by 20−40 $cm^{-1}$ (*i.e.*, at ~1650−1670 $cm^{-1}$).[30,38−40] Most interestingly, these frequencies correspond approximately to those found for the component bands of CFGAILSS-capped nanoparticles, indicating the formation of parallel $\beta$-sheets, especially in the capping layer of the larger nanoparticles. However, the frequencies and widths and particularly the relative strengths of the two bands do not completely conform to expectation. This is due to two effects, which will be discussed in detail in the following: (i) the dependence of the $\beta$-sheet amide I′ eigenmodes on sheet size and (ii) the surface selection rules.

The sensitivity of the amide I′ band to peptide secondary structure is largely due to dipole−dipole coupling of the amide I′ vibrations of neighboring amide groups, which strongly depends on their relative geometry. For an infinitely extended parallel $\beta$-sheet structure, it can be shown by basic theoretical considerations that only two of the resulting vibrational eigenmodes are IR-active, with a dominant band at lower frequency which is polarized orthogonal to the peptide backbone and a much weaker band at higher frequency which is polarized parallel to the backbone.[42,43] Simulations based on dipole−dipole coupling[38,39] or *ab initio* quantum chemical methods[40] show that, for sheets consisting of less than ~7 parallel chains, the observable eigenfrequencies change measurably without greatly affecting the polarization direction of the main modes; in particular, a further decrease in the number of chains results in a shift of the dominant low-frequency band to higher frequencies, whereas the high-frequency band is much less affected.

For the SAMs investigated here, the curvature of the anchoring surface frustrates the formation of extended parallel $\beta$-sheets, and the constraint becomes more stringent with decreasing nanoparticle size. We present a simple geometrical model to illustrate this effect (Figure 4). Under the hypotheses of this model, the maximum numbers of adjacent peptides in a sheet are, respectively, 3, 5, and 11 for the 5, 10, and 25 nm diameter nanoparticles.[44] We suggest that this is the reason for the slightly higher frequency of the observed low-frequency band, compared to typical values for parallel $\beta$-sheets, and the observed shift of this band with nanoparticle size (25 nm NPs, 1637 $cm^{-1}$; 10 nm NPs, 1639 $cm^{-1}$); in agreement with this suggestion, the observed high-frequency band position is largely constant, as judged from the second derivative spectra. Structural inhomogeneity within the SAM, that is, the occurrence of parallel $\beta$-sheets with different number of strands, will furthermore lead to a broadening of the amide I′ band, which should be most pronounced for the high curvature anchoring surface of smaller nanoparticles, in agreement with our observations. The curvature effect on molecular conformation observed here is reminiscent of the increase of the gauche defects in alkyl chains ligands observed by vibrational sum frequency generation when the size of the nanoparticle decreases.[45] Other causes for inhomogeneity include the polydispersity and polymorphism within each sample, as well as the existence on each particles of nonequivalent binding sites corresponding to different crystal faces, terraces, and vertices.[46,47] Further experimental and theoretical investigations will be required to fully account for these effects. As shown in Figure 4A, the dimension of the gold atom is in the same range as the other critical lengths in this problem, so it is likely that atomic details of the surface, ignored here in first approximation, will contribute to the final molecular structure.

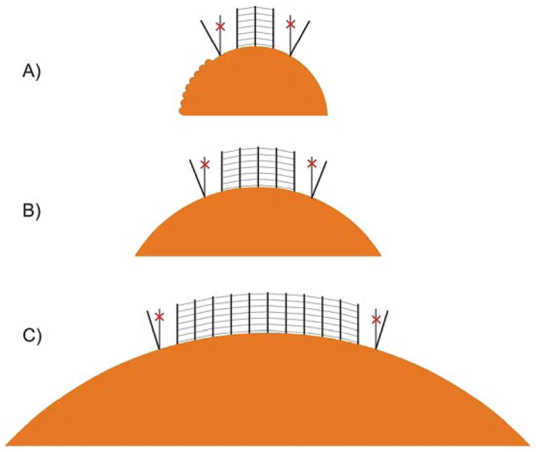


**Figure 4. Geometrical constraints for the formation of parallel arrays of peptides on spherical nanoparticles. Particles of (A) 5 nm, (B) 10 nm, and (C) 25 nm diameter are represented with hypothetical parallel peptides anchored with a constant arc separation of 0.63 nm (corresponding to 1/(capping density)$^{1/2}$).[41] The hydrogen bonding network is shown with dotted lines between adjacent peptides and is deemed to break when the vertical mismatch between adjacent peptides exceeds 0.15 nm, *i.e.*, 50% of the distance between two residues in a peptide strand in $\beta$-sheet configuration (numbers used to draw the figure are provided in the Supporting Information). As a first approximation, the gold surface is represented as a smooth spherical surface; however, this is a serious oversimplification as the diameter of the gold atoms is in the same size range as other characteristic lengths of this problem. Some surface gold atoms are shown to scale in (A).**

The IR spectra of small molecules attached to a metal surface are furthermore subject to the surface selection rules, which state that only vibrations whose dipole moment change has a significant component orthogonal to the surface are IR-active. This effect arises from the high conductivity of metals, which rules out the existence of electric field components parallel to the surface. It has been shown theoretically[16] and experimentally[48] that the surface selection rule is also valid at the surface of metal nanoparticles, at least up to distances which are comparable to the particle size. This does significantly affect the IR spectra of peptides attached to gold nanoparticles. In particular, for peptides which are anchored to the nanoparticle by one of their termini and form parallel $\beta$-sheet structures, the low-frequency amide I′ mode, which normally dominates the IR spectrum but is polarized orthogonal to the peptide backbone and thus parallel to the nanoparticle surface, will be strongly suppressed; on the other hand, the high-frequency mode, polarized parallel to the backbone and thus orthogonal to the surface, will be enhanced. This distorting effect will be particularly pronounced for peptides anchored to larger nanoparticles but also for the inner section of peptides on the smaller nanoparticles. For the

CFGAILSS peptide, which in the extended $\beta$-sheet conformation has a length of 3 nm, this effect is significant for the full length of the peptide when attached to nanoparticles with a diameter of 25 nm. The quantitative treatment of Greenler *et al.*[16] shows that for this case at the end of the peptide the IR absorbance of vibrations parallel to the nanoparticle surface is suppressed by a factor of 35 compared to that of vibrations orthogonal to the surface, with an even larger suppression closer to the nanoparticle surface. For nanoparticles with 10 or 5 nm diameter, the effect is somewhat weaker, with a suppression by only a factor of 6 or 2, respectively, at the end of the peptide, but still very large close to the surface. It is, therefore, not surprising that the high-frequency band is of similar strength as the low-frequency band in the FTIR spectra of CFGAILSS-capped nanoparticles.

Taking into account this distorting effect of the surface selection rules, the observed amide I′ spectra for the CFGAILSS capping layer, with their distinct two bands near 1665 and ~1640 $cm^{-1}$, confirm the formation of parallel $\beta$-sheet structure. These bands are clearly visible for nanoparticles with 10 or 25 nm diameter, but even in the spectrum for 5 nm nanoparticles, there is some indication for these bands (see Figure 3D), indicating the formation of at least partial $\beta$-sheet structure. It has to be noted that the total amide I′ absorbance of residues in $\beta$-sheet conformation near the nanoparticle surface is significantly reduced because of the suppression of the strong absorbance of the low-frequency mode due to the surface selection rules, whereas contributions from disordered peptide structure is much less affected due to the random orientation of the amide I′ dipole moment with respect to the nanoparticle surface. Thus, the FTIR spectra shown in Figure 3B are likely to significantly *under*estimate the $\beta$-sheet content of the CFGAILSS capping layer.

To further confirm the interpretation of the FTIR measurements, we used solid-state NMR as an alternative independent experimental approach.

**Solid-State NMR Investigation of CALNN-Capped and CFGAILSS-Capped Nanoparticles.** Figure 5 shows a $^{13}C$ CP-MAS spectrum of 5 nm gold nanoparticles capped with a 1:1 mixture of [$^{13}C'$-A]CFGAILSS and [$^{13}C\alpha$-A]-CFGAILSS. The peaks are somewhat broader than observed for the fibrils (Table 1, Figure 1C), and the increased line widths may originate from the properties of the nanoparticles or from structural disorder in the peptide molecules around the labeled sites. NMR studies of alkanethiolate-capped gold nanoparticles revealed that the $^{13}C$ lines are broadest for carbon sites closest to the Au core,[49] and line widths also increase with increasing particle size.[50] This systematic effect has been attributed to inhomogeneous broadening as a result of variations in the Au ligand site,

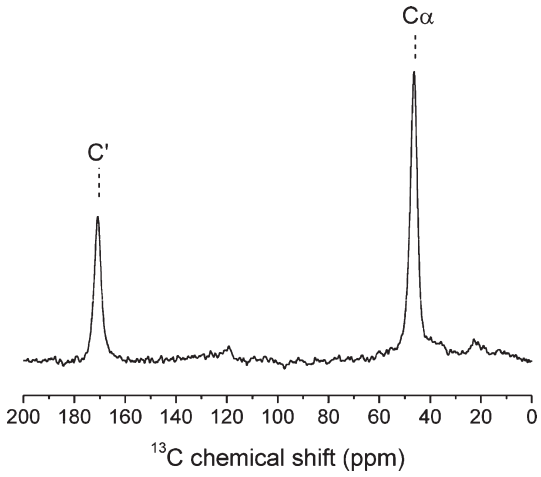


**Figure 5. $^{13}C$ CP-MAS NMR spectrum of 5 nm gold nanoparticles capped with 1:1 [$^{13}C'$-A]CFGAILSS/[$^{13}C\alpha$-A]-CFGAILSS.**

giving rise to distributions of chemical shifts.[49,50] A distribution of weak Knight shifts may also contribute to the broadening effect.[51] Knight shifts could arise from the interaction of conductance electrons of the Au cluster with the $^{13}C$ nuclei of the peptide, and this phenomenon is known to increase with the density and/or size of the particles.[49] Indeed, substantially broader lines are seen for 10 nm nanoparticles capped with a 1:1 mixture of [$^{13}C'$-A]CFGAILSS and [$^{13}C\alpha$-A]CFGAILSS (Table 1), consistent with the broadening effect being related to the size and metallic properties of the particles.

We then turned to dipolar coupling experiments, using first the CFGAILSS fibrils as a reference. Spectra of [$^{13}C'$-A]CFGAILSS/[$^{13}C\alpha$-A]CFGAILSS fibrils obtained in a rotational resonance experiment can be seen in Figure 6. The decrease in the signal intensities with increasing mixing time indicates that distance-dependent dipolar couplings occur between $^{13}C'$ and $^{13}C\alpha$ of neighboring peptides. Comparison of the exchange measurements with numerically simulated curves (Figure 6B) yields a dipolar coupling constant which translates into an intermolecular $^{13}C'-^{13}C\alpha$ distance $r_{CC}$ of 5.0 $\pm$ 0.3 Å. Such a short distance is possible if $\beta$-strands are in-register along the hydrogen bonding axis of the fibrils; that is, each N−H of Ala5 forms an intermolecular hydrogen bond with C═O of the same residue when in an antiparallel alignment (Figure 6C).

Rotational resonance spectra of 5 nm gold nanoparticles capped with a 1:1 mixture of [$^{13}C'$-A]CFGAILSS and [$^{13}C\alpha$-A]CFGAILSS spectra show a decline in peak intensities with increasing mixing time, similar to the spectra of the fibrillar sample (Figure 7A). No change in the peak intensities occurs away from a rotational resonance (RR) condition (Figure 7B), confirming that the effect is related to dipolar coupling between $^{13}C'$ and $^{13}C\alpha$ of neighboring peptides on the particle

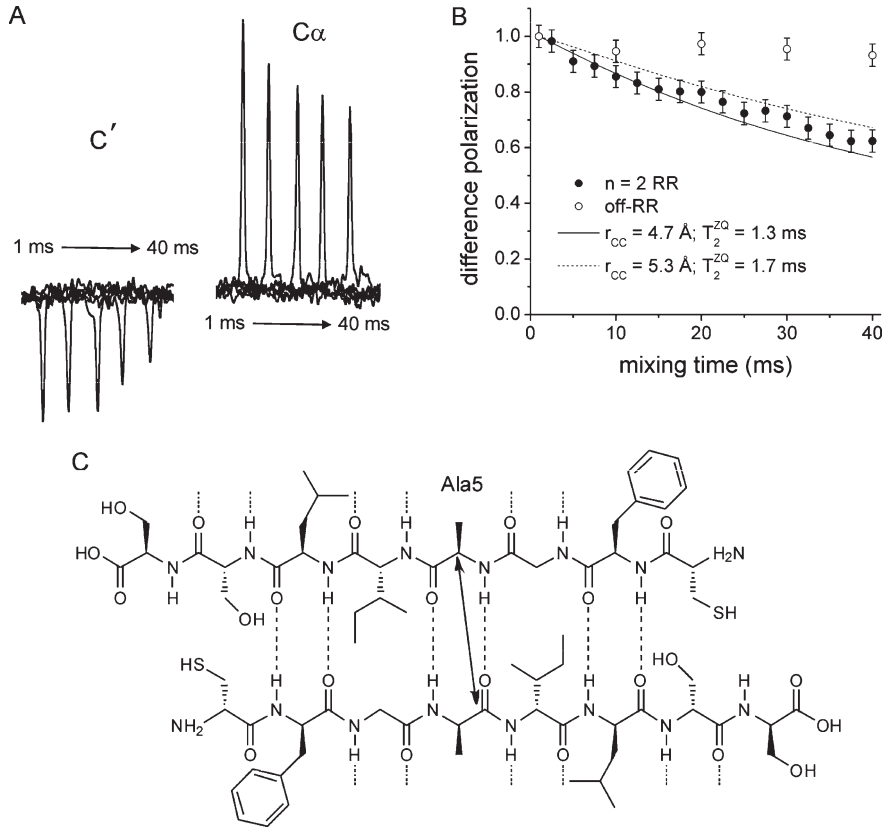


**Figure 6. Measurement of $^{13}C'-^{13}C\alpha$ dipolar couplings in 1:1 [$^{13}C'$-A]CFGAILSS/[$^{13}C\alpha$-A]CFGAILSS fibrils using rotational resonance NMR. (A) Spectra of fibrils obtained using the constant time experiment described in Figure S2. Peaks for C′ and Cα are shown, from left to right, for mixing times ($\tau_m$) of 1, 10, 20, 30, and 40 ms at a MAS frequency of 6254 Hz, which satisfies the $n = 2$ RR condition. (B) Plot of magnetization exchange, as represented by difference intensities for the C′ and Cα peaks over a range of mixing times. Data are shown for $n = 2$ RR (filled circles) and for a MAS rate (5200 Hz) away from a RR condition (open circles). Error bars represent the level of the noise. Solid and dashed lines are numerically simulated curves bounding the upper and lower error limits of the $n = 2$ RR data and correspond to the C′−Cα distances and $T_2^{ZQ}$ values indicated. (C) Model of an antiparallel configuration with Ala5 in-register. The double arrow indicates the interatomic distance measured.**

surface. If it is assumed that all peptides are distributed at regular intervals in a uniform matrix, the exchange measurements are again consistent with an intermolecular $^{13}C'-^{13}C\alpha$ distance of 4.9 ± 0.3 Å (Figure S3A). The peptide molecules are attached to the nanoparticles *via* their N-terminal cysteine residue and so are unable to assemble into the antiparallel $\beta$-strand arrangement adopted in the fibrils. The short $^{13}C'-^{13}C\alpha$ distance is possible, however, if the peptide molecules are organized in an in-register, parallel arrangement with N−H of Ala5 hydrogen bonded to C═O of Gly4. Interestingly, rotational resonance spectra of 5 nm particles capped with 1:1 [$^{13}C'$-A]CALNN/[$^{13}C\alpha$-A]CALNN are unresponsive over the same mixing times (Figure 7C,D), indicating that the dipolar coupling is weak and the intermolecular separation of $^{13}C'$ and $^{13}C\alpha$ is substantially greater than for the CFGAILSS nanoparticles. Rotational resonance spectra for 10 nm gold nanoparticles capped with a 1:1 mixture of [$^{13}C'$-A]CFGAILSS and [$^{13}C\alpha$-A]CFGAILSS (Figure 7E) are again consistent with an intermolecular C′−Cα distance of 5.0 ± 0.3 Å (Figure S3B). Spectra of 10 nm particles capped with 1:1 [$^{13}C'$-A]CALNN/[$^{13}C\alpha$-A]CALNN show no evidence of magnetization exchange (not presented).

Given that CALNN and CFGAILSS have very similar capping density (2.55 and 2.4 peptides per nm$^2$, respectively), the presence of dipolar coupling observed indicates a difference in the molecular conformations of these peptides. If we consider a locally hexagonal close-packed structure with a packing density of 2.55 peptides per nm$^2$, the intermolecular distance would be 0.67 nm, that is, larger than the intermolecular distances measured above. In addition, if we take into account the fact that the labeled alanines are not in direct contact with the surface, the predicted average distance becomes even larger. In other words, it is clear that the intermolecular distances observed in the CFGAILSS monolayer cannot be explained simply by a confinement in a dense layer but rather originates from local oriented intermolecular hydrogen bonding which occurs in the CFGAILSS layer but not in the CALNN layer. An interesting, and potentially useful, outcome of this work is that,

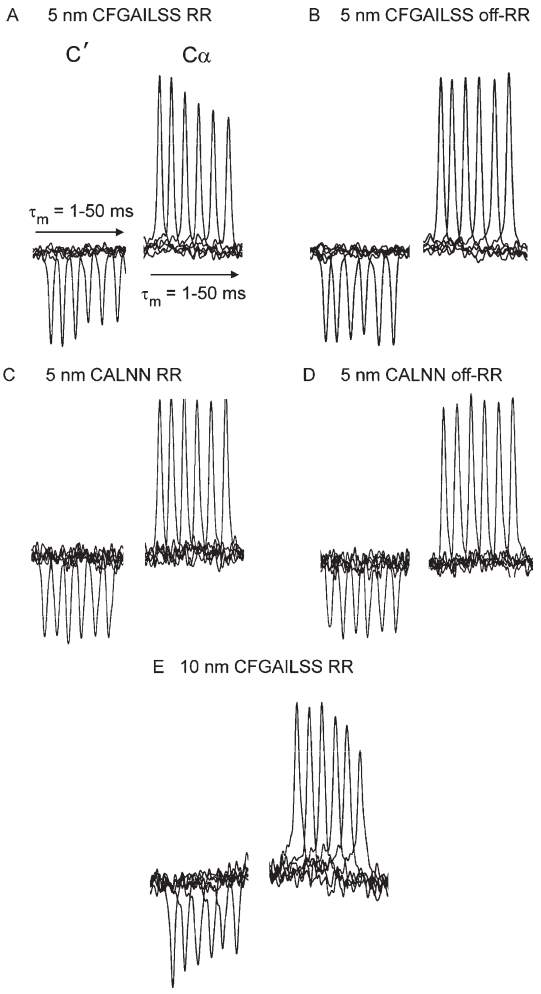


**Figure 7. Detection of $^{13}C'-^{13}C\alpha$ dipolar couplings in peptide-capped gold nanoparticles using rotational resonance NMR. Peaks for C′ and Cα are shown, from left to right, for mixing times ($\tau_m$) of 1, 10, 20, 30, 40, and 50 ms at MAS frequencies satisfying the $n$ = 2 RR condition. Top row: spectra for 5 nm particles capped with 1:1 [$^{13}$C′-A]-CFGAILSS/[$^{13}$Cα-A]CFGAILSS at $n$ = 2 RR (A) and off-RR (B). Middle row: spectra for 5 nm particles capped with 1:1 [$^{13}$C′-A]CALNN/[$^{13}$Cα-A]CALNN at $n$ = 2 RR (C) and off-RR (D). Bottom row: spectra for 10 nm particles capped with 1:1 [$^{13}$C′-A]CFGAILSS/[$^{13}$Cα-A]CFGAILSS at $n$ = 2 RR (E).**

whereas free CFGAILSS aggregates into amyloid-like fibrils spontaneously and rapidly, aggregation of the CFGAILSS-capped nanoparticles does not occur. Protein and peptide fibril structures are stabilized by generic intermolecular hydrogen bonds and also by specific packing interactions between amino acid side groups of two or more $\beta$-sheet layers constituting a so-called cross-$\beta$ spine.[52] It appears from the results here that all of the required intermolecular interactions are satisfied *within* each nanoparticle, thus preventing interdigitating peptide interactions *between* nanoparticles. The ability of CFGAILSS to form distinct supramolecular assemblies within individual nanoparticles is a potentially valuable property which could be exploited for novel purposes.

## CONCLUSIONS

Using a combination of FTIR and rotational resonance NMR spectroscopy, we have demonstrated that the two cysteine-terminated peptides CALNN and CFGAILSS adopt different molecular conformations at the surface of nanoparticles. CALNN is random coil both in solution and when attached to gold nanoparticles. CFGAILSS is forming extended amyloid fibrils in aqueous solutions with an antiparallel $\beta$-sheet structure. When constrained to a nanoparticle surface, it has a curvature-dependent tendency to form parallel $\beta$-sheets with hydrogen bonding between adjacent peptides. While determining the structure of small molecules at the surface of nanoparticles remains a major challenge, our study shows that FTIR and ssNMR spectroscopy can provide detailed insights into the structure and intermolecular interactions. Whereas FTIR spectroscopy yields information on the overall secondary structure of the peptide capping layer, ssNMR spectroscopy is sensitive to local structure and allows one to measure the distances between labeled residues. In the future, CALNN, CFGAILSS, and other peptides that will be designed and characterized with similar methods will constitute a library of elements with well-defined structures and intermolecular interactions, which could be used as building blocks for the rational design of protein-like nanoparticles with multiple domains and complex functions.

## MATERIALS AND METHODS

Complete materials and methods are provided in the Supporting Information. A summary is given here.

**Peptides.** For NMR studies, the CFGAILSS and CALNN peptides were each labeled with $^{13}$C at either the amide carbon (C′) or the α-carbon (Cα) of the single alanine residue (*i.e.*, [$^{13}$C′−A]-CFGAILSS, [$^{13}$C′-A]CALNN, [$^{13}$Cα-A]CFGAILSS, and [$^{13}$Cα-A]-CALNN).

**Synthesis of 5, 8, 10, and 25 nm Diameter Gold Nanoparticles.** Nanoparticles were prepared by aqueous reduction of $HAuCl_4$. Sodium acrylate and tannic acid were used for the preparation of 5, 8, and 10 nm nanoparticles. A two-step seeding method[53] was used to obtain the 25 nm diameter nanoparticles.

**Preparation of Peptide-Capped Nanoparticles.** Because of the high peptide concentration required for NMR and FTIR studies, the samples were prepared by mixing the appropriate peptide solution with 100 mL of nanoparticle suspension for FTIR and 250 mL for solid-state NMR. For the preparation of the CFGAILSS nanoparticles, a two-step capping procedure was used to dissolve fibers and promote formation of the SAM. Those samples were then purified (removal of excess peptide), concentrated, lyophilized, and resuspended in 200 $\mu$L of $D_2O$ for FTIR studies or 100 $\mu$L of $H_2O$ for NMR.

**Fourier Transform Infrared Spectroscopy: Data Acquisition and Treatment.** The samples in $D_2O$ were loaded into a FTIR cell consisting of two $CaF_2$ windows separated by a 50 $\mu$m PTFE spacer. FTIR spectra were recorded using a BioRad FTS-40 spectrometer with

a HgCdTe (MCT) detector. A nominal resolution of 1 $cm^{-1}$ was used throughout, and all spectra were averaged over 500 scans. The spectrometer was purged with dry air; any residual water vapor absorption was corrected for by subtracting an appropriately scaled spectrum of humid air. Solvent correction was performed by subtracting a spectrum of $D_2O$, measured under the same conditions as peptide/nanoparticle samples, and appropriately scaled to achieve a flat baseline in the region 1800−2000 $cm^{-1}$.

For calculating the second derivative spectra shown in Figure 3, the spectra had to be numerically smoothed to remove artifacts arising from noise and residual water vapor lines, effectively reducing the resolution to ~7 $cm^{-1}$; all spectra were subjected to the same smoothing process.

**Solid-State NMR: $^{13}C$ Cross-Polarization Magic-Angle Spinning. (**CP-MAS) NMR experiments were performed with a Bruker Avance 400 spectrometer operating at a magnetic field of 9.3 T. Hydrated fibril or nanoparticle samples were packed into a 4 mm zirconium rotor and rotated at a MAS frequency of between 6 and 7 kHz (±1 Hz). All experiments utilized an initial 4.0 $\mu$s $^1H$ 90° excitation pulse, 1 ms Hartmann−Hahn contact time at a $^1H$ spin-lock field of 65 kHz, 85 kHz TPPM proton decoupling,[54] and a 2 s recycle delay.

**. Constraints on $^{13}C-^{13}C$ Interatomic Distances** were obtained by measuring magnetization exchange at $n = 2$ rotational resonance (RR) using the constant time pulse sequence described by Balazs and Thompson.[55] The variable time pulse sequence used routinely for RR measurements (Figure S2a in the Supporting Information) can give rise to different amounts of heat being absorbed by the gold particles as a result of increasing exposure to high-power irradiation (*i.e.*, proton decoupling) in experiments with longer mixing times. Sample heating could affect the measured signal intensities and prevent the accurate measurement of dipolar couplings. In the constant time pulse scheme (Figure S2b), the mixing time $\tau_m$ is varied as normal but the overall duration of proton decoupling ($\tau_c$), and hence the heat absorbed by the sample, remains the same in each experiment. As an extra precaution against sample heating, the temperature was reduced to −40 °C, which has the further advantage of reducing interference from molecular dynamics.

Magnetization exchange was measured by adjusting the sample spinning rate ($\omega_R$) to half the frequency difference of the pair of spins selected (*i.e.*, $n = 2$ RR). Measurements at $n = 1$ RR were not attempted for nanoparticle samples because higher MAS frequencies tended to give rise to frictional heating which severely attenuated the signal. A series of experiments at mixing times $\tau_m$ of up to 50 ms was performed to measure the time dependence of difference polarization. Data representing exchange of Zeeman order ("magnetization exchange curves") were obtained from the difference in intensities of each pair of peaks. Spectra were processed with 20 Hz exponential line broadening.

**Numerical Simulations of Magnetization Exchange Curves.** The internuclear distance ($r_{CC}$) between the C′ and Cα spins of Ala5 at $n = 2$ RR were determined from numerical simulations of magnetization exchange curves using a Fortran computer program written specifically for this purpose. Curves were calculated as described elsewhere[56,57] and are a function of the distance-dependent $^{13}C-^{13}C$ dipolar coupling constant $d_{\chi\chi}$ and the zero quantum relaxation time $T_2^{ZQ}$. Values for $^{13}C$ chemical shift anisotropy and asymmetry parameters were measured from solid alanine. Simulations took into account the statistical frequency of adjacent peptides in the fibrillar or nanoparticle matrix being labeled the same site and therefore unable to participate in magnetization exchange. The value of $T_2^{ZQ}$ is not known but is routinely estimated from the reciprocal sum of the two line widths; in this case, for C′ and Cα. A series of curves was calculated for a range of $T_2^{ZQ}$ values in which the upper and lower limits corresponded to half the sum of the line widths and twice the sum of the line widths, respectively. Values of $r_{CC}$ and $T_2^{ZQ}$ were taken from the simulated curves, giving the best fit to the upper and lower error limits of the experimental data.

*Conflict of Interest:* The authors declare no competing financial interest.

*Acknowledgment.* The authors acknowledge support from the Biotechnology and Biological Sciences Research Council Grant BB/D020638/1 (David Phillips Fellowship to R.L.) and the Engineering and Physical Sciences Research Council (EP/H046143).

*Supporting Information Available:* Materials and methods (nanoparticle preparation, FTIR, solid-state NMR CP-MAS and rotational resonance). Supporting Information Figures S1−S3 (TEM, UV−visible spectra, and size distribution of nanoparticles; pulse sequences for rotational resonance and numerical simulations of magnetization exchange curves). Spreadsheet for the preparation of Figure 4. This material is available free of charge *via* the Internet at http://pubs.acs.org.

## REFERENCES AND NOTES

1. Boal, A. K.; Rotello, V. M. Fabrication and Self-Optimization of Multivalent Receptors on Nanoparticle Scaffolds. *J. Am. Chem. Soc.* **2000**, *122*, 734–735.
2. Ionita, P.; Volkov, A.; Jeschke, G.; Chechik, V. Lateral Diffusion of Thiol Ligands on the Surface of Au Nanoparticles: An Electron Paramagnetic Resonance Study. *Anal. Chem.* **2008**, *80*, 95–106.
3. Gentilini, C.; Franchi, P.; Mileo, E.; Polizzi, S.; Lucarini, M.; Pasquato, L. Formation of Patches on 3D SAMs Driven by Thiols with Immiscible Chains Observed by ESR Spectroscopy. *Angew. Chem., Int. Ed.* **2009**, *48*, 3060–3064.
4. Jadzinsky, P. D.; Calero, G.; Ackerson, C. J.; Bushnell, D. A.; Kornberg, R. D. Structure of a Thiol Monolayer-Protected Gold Nanoparticle at 1.1 Angstrom Resolution. *Science* **2007**, *318*, 430–433.
5. Wang, Y.; Neyman, A.; Arkhangelsky, E.; Gitis, V.; Meshi, L.; Weinstock, I. A. Self-Assembly and Structure of Directly Imaged Inorganic-Anion Monolayers on a Gold Nanoparticle. *J. Am. Chem. Soc.* **2009**, *131*, 17412–17422.
6. Duchesne, L.; Wells, G.; Fernig, D. G.; Harris, S. A.; Levy, R. Supramolecular Domains in Mixed Peptide Self-Assembled Monolayers on Gold Nanoparticles. *ChemBioChem* **2008**, *9*, 2127–2134.
7. Jackson, A. M.; Myerson, J. W.; Stellacci, F. Spontaneous Assembly of Subnanometre-Ordered Domains in the Ligand Shell of Monolayer-Protected Nanoparticles. *Nat. Mater.* **2004**, *3*, 330–336.
8. Cesbron, Y.; Shaw, C. P.; Birchall, J.; Free, P.; Levy, R. Stripy Nanoparticle Revisited. *Small*, Under review.
9. Pasquato, L.; Pengo, P.; Scrimin, P. Nanozymes: Functional Nanoparticle-Based Catalysts. *Supramol. Chem.* **2005**, *17*, 163–171.
10. Mastroianni, A. J.; Claridge, S. A.; Alivisatos, A. P. Pyramidal and Chiral Groupings of Gold Nanocrystals Assembled Using DNA Scaffolds. *J. Am. Chem. Soc.* **2009**, *131*, 8455–8459.
11. Sardar, R.; Shumaker-Parry, J. S. Asymmetrically Functionalized Gold Nanoparticles Organized in One-Dimensional Chains. *Nano Lett.* **2008**, *8*, 731–736.
12. Levy, R.; Thanh, N. T. K.; Doty, R. C.; Hussain, I.; Nichols, R. J.; Schiffrin, D. J.; Brust, M.; Fernig, D. G. Rational and Combinatorial Design of Peptide Capping Ligands for Gold Nanoparticles. *J. Am. Chem. Soc.* **2004**, *126*, 10076–10084.
13. Maran, F.; Fabris, L.; Antonello, S.; Armelao, L.; Donkers, R. L.; Polo, F.; Toniolo, C. Gold Nanoclusters Protected by Conformationally Constrained Peptides. *J. Am. Chem. Soc.* **2006**, *128*, 326–336.
14. Rio-Echevarria, I. M.; Tavano, R.; Causin, V.; Papini, E.; Mancin, F.; Moretto, A. Water-Soluble Peptide-Coated Nanoparticles: Control of the Helix Structure and Enhanced Differential Binding to Immune Cells. *J. Am. Chem. Soc.* **2011**, *133*, 8–11.
15. Olmedo, I.; Araya, E.; Sanz, F.; Medina, E.; Arbiol, J.; Toledo, P.; Alvarez-Lueje, A.; Giralt, E.; Kogan, M. J. How Changes in the Sequence of the Peptide Clpffd-$NH_2$ Can Modify the Conjugation and Stability of Gold Nanoparticles and Their Affinity for $\beta$-Amyloid Fibrils. *Bioconjugate Chem.* **2008**, *19*, 1154–1163.
16. Greenler, R. G.; Snider, D. R.; Witt, D.; Sorbello, R. S. The Metal-Surface Selection Rule for Infrared-Spectra of

Molecules Adsorbed on Small Metal Particles. *Surf. Sci.* **1982**, *118*, 415–428.
17. Kraatz, H. B.; Mandal, H. S. Effect of the Surface Curvature on the Secondary Structure of Peptides Adsorbed on Nanoparticles. *J. Am. Chem. Soc.* **2007**, *129*, 6356.
18. Serizawa, T.; Hirai, Y.; Aizawa, M. Novel Synthetic Route to Peptide-Capped Gold Nanoparticles. *Langmuir* **2009**, *25*, 12229–12234.
19. Tan, Y. N.; Lee, J. Y.; Wang, D. I. C. Uncovering the Design Rules for Peptide Synthesis of Metal Nanoparticles. *J. Am. Chem. Soc.* **2010**, *132*, 5677–5686.
20. Chen, C. L.; Rosi, N. L. Peptide-Based Methods for the Preparation of Nanostructured Inorganic Materials. *Angew. Chem., Int. Ed.* **2010**, *49*, 1924–1942.
21. Slocik, J. M.; Naik, R. R. Probing Peptide−Nanomaterial Interactions. *Chem. Soc. Rev.* **2010**, *39*, 3454–3463.
22. Irvine, G. B.; El-Agnaf, O. M.; Shankar, G. M.; Walsh, D. M. Protein Aggregation in the Brain: The Molecular Basis for Alzheimer's and Parkinson's Diseases. *Mol. Med.* **2008**, *14*, 451–464.
23. Ferreira, S. T.; Vieira, M. N. N.; De Felice, F. G. Soluble Protein Oligomers as Emerging Toxins in Alzheimer's and Other Amyloid Diseases. *IUBMB Life* **2007**, *59*, 332–345.
24. Tenidis, K.; Waldner, M.; Bernhagen, J.; Fischle, W.; Bergmann, M.; Weber, M.; Merkle, M. L.; Voelter, W.; Brunner, H.; Kapurniotu, A. Identification of a Penta- and Hexapeptide of Islet Amyloid Polypeptide (Iapp) with Amyloidogenic and Cytotoxic Properties. *J. Mol. Biol.* **2000**, *295*, 1055–1071.
25. Madine, J.; Jack, E.; Stockley, P. G.; Radford, S. E.; Serpell, L. C.; Middleton, D. A. Structural Insights into the Polymorphism of Amyloid-like Fibrils Formed by Region 20−29 of Amylin Revealed by Solid-State NMR and X-ray Fiber Diffraction. *J. Am. Chem. Soc.* **2008**, *130*, 14990–15001.
26. Barth, A.; Zscherp, C. What Vibrations Tell Us About Proteins. *Q. Rev. Biophys.* **2002**, *35*, 369–430.
27. Cheatum, C. M.; Tokmakoff, A.; Knoester, J. Signatures of $\beta$-Sheet Secondary Structures in Linear and Two-Dimensional Infrared Spectroscopy. *J. Chem. Phys.* **2004**, *120*, 8201–8215.
28. Krimm, S.; Abe, Y. Intermolecular Interaction Effects in Amide I Vibrations of Beta Polypeptides. *Proc. Natl. Acad. Sci. U.S.A.* **1972**, *69*, 2788–2792.
29. Byler, D. M.; Susi, H. Examination of the Secondary Structure of Proteins by Deconvolved FTIR Spectra. *Biopolymers* **1986**, *25*, 469–487.
30. Arrondo, J. L. R.; Muga, A.; Castresana, J.; Goni, F. M. Quantitative Studies of the Structure of Proteins in Solution by Fourier-Transform Infrared-Spectroscopy. *Prog. Biophys. Mol. Biol.* **1993**, *59*, 23–56.
31. Wulandari, P.; Li, X. H.; Tamada, K.; Hara, M. Conformational Study of Citrates Adsorbed on Gold Nanoparticles Using Fourier Transform Infrared Spectroscopy. *J. Nonlinear Opt. Phys. Mater.* **2008**, *17*, 185–192.
32. Free, P.; Shaw, C. P.; Levy, R. PEGylation Modulates the Interfacial Kinetics of Proteases on Peptide-Capped Gold Nanoparticles. *Chem. Commun.* **2009**, 5009–5011.
33. Levy, R.; Wang, Z. X.; Duchesne, L.; Doty, R. C.; Cooper, A. I.; Brust, M.; Fernig, D. G. A Generic Approach to Monofunctionalized Protein-like Gold Nanoparticles Based on Immobilized Metal Ion Affinity Chromatography. *ChemBioChem* **2006**, *7*, 592–594.
34. Levy, R. Peptide-Capped Gold Nanoparticles: Towards Artificial Proteins. *ChemBioChem* **2006**, *7*, 1141–1145.
35. Stine, W. B.; Dahlgren, K. N.; Krafft, G. A.; LaDu, M. J. *In Vitro* Characterization of Conditions for Amyloid-$\beta$ Peptide Oligomerization and Fibrillogenesis. *J. Biol. Chem.* **2003**, *278*, 11612–11622.
36. Hostetler, M. J.; Templeton, A. C.; Murray, R. W. Dynamics of Place-Exchange Reactions on Monolayer-Protected Gold Cluster Molecules. *Langmuir* **1999**, *15*, 3782–3789.
37. Duchesne, L.; Gentili, D.; Comes-Franchini, M.; Fernig, D. G. Robust Ligand Shells for Biological Applications of Gold Nanoparticles. *Langmuir* **2008**, *24*, 13572–13580.
38. Chirgadze, Y. N.; Nevskaya, N. A. Infrared-Spectra and Resonance Interaction of Amide-One Vibration of Parallel-Chain Pleated Sheet. *Biopolymers* **1976**, *15*, 627–636.
39. Hahn, S.; Kim, S. S.; Lee, C.; Cho, M. Characteristic Two-Dimensional IR Spectroscopic Features of Antiparallel and Parallel $\beta$-Sheet Polypeptides: Simulation Studies. *J. Chem. Phys.* **2005**, 123.
40. Kubelka, J.; Keiderling, T. A. Differentiation of $\beta$-Sheet-Forming Structures: *Ab Initio*-Based Simulations of IR Absorption and Vibrational CD for Model Peptide and Protein $\beta$-Sheets. *J. Am. Chem. Soc.* **2001**, *123*, 12048–12058.
41. Instead of 0.63 nm (measured average distance), an interstrand distance of 0.48 nm (parrallel $\beta$-sheets) could have been used in this geometrical model. Given the lack of atomic level information on anchoring of the peptides on the nanoparticle surface, this choice is somewhat arbitrary. Both models lead to the same conclusion, *i.e.*, that the size of those domains is limited and curvature-dependent.
42. Miyazawa, T. Perturbation Treatment of the Characteristic Vibrations of Polypeptide Chains in Various Configurations. *J. Chem. Phys.* **1960**, *32*, 1647–1652.
43. Barth, A. Selective Monitoring of 3 out of 50,000 Protein Vibrations. *Biopolymers* **2002**, *67*, 237–241.
44. If we use an arc distance of 0.48 nm (see ref 41 above), the numbers are 5, 7, and 17 instead of 3, 5, and 11.
45. Weeraman, C.; Yatawara, A. K.; Bordenyuk, A. N.; Benderskii, A. V. Effect of Nanoscale Geometry on Molecular Conformation: Vibrational Sum-Frequency Generation of Alkanethiols on Gold Nanoparticles. *J. Am. Chem. Soc.* **2006**, *128*, 14244–14245.
46. Guo, R.; Song, Y.; Wang, G. L.; Murray, R. W. Does Core Size Matter in the Kinetics of Ligand Exchanges of Monolayer-Protected Au Clusters? *J. Am. Chem. Soc.* **2005**, *127*, 2752–2757.
47. Luedtke, W. D.; Landman, U. Structure and Thermodynamics of Self-Assembled Monolayers on Gold Nanocrystallites. *J. Phys. Chem. B* **1998**, *102*, 6566–6572.
48. Lee, S. J.; Han, W. H.; Kim, K. Perfluorocarbon-Stabilized Silver Nanoparticles Manufactured from Layered Silver Carboxylates. *Chem. Commun.* **2002**, 442–443.
49. Hostetler, M. J.; Wingate, J. E.; Zhong, C. J.; Harris, J. E.; Vachet, R. W.; Clark, M. R.; Londono, J. D.; Green, S. J.; Stokes, J. J.; Wignall, G. D.; *et al.* Alkanethiolate Gold Cluster Molecules with Core Diameters from 1.5 to 5.2 nm: Core and Monolayer Properties as a Function of Core Size. *Langmuir* **1998**, *14*, 17–30.
50. Badia, A.; Gao, W.; Singh, S.; Demers, L.; Cuccia, L.; Reven, L. Structure and Chain Dynamics of Alkanethiol-Capped Gold Colloids. *Langmuir* **1996**, *12*, 1262–1269.
51. Kohlmann, O.; Steinmetz, W. E.; Mao, X. A.; Wuelfing, W. P.; Templeton, A. C.; Murray, R. W.; Johnson, C. S. NMR Diffusion, Relaxation, and Spectroscopic Studies of Water Soluble, Monolayer-Protected Gold Nanoclusters. *J. Phys. Chem. B* **2001**, *105*, 8801–8809.
52. Nelson, R.; Sawaya, M. R.; Balbirnie, M.; Madsen, A. O.; Riekel, C.; Grothe, R.; Eisenberg, D. Structure of the Cross-$\beta$ Spine of Amyloid-like Fibrils. *Nature* **2005**, *435*, 773–778.
53. Cooper, A. I.; Hussain, I.; Brust, M.; Papworth, A. J. Preparation of Acrylate-Stabilized Gold and Silver Hydrosols and Gold−Polymer Composite Films. *Langmuir* **2003**, *19*, 4831–4835.
54. Bennett, A. E.; Rienstra, C. M.; Auger, M.; Lakshmi, K. V.; Griffin, R. G. Heteronuclear Decoupling in Rotating Solids. *J. Chem. Phys.* **1995**, *103*, 6951.
55. Balazs, Y. S.; Thompson, L. K. Practical Methods for Solid-State NMR Distance Measurements on Large Biomolecules: Constant-Time Rotational Resonance. *J. Magn. Reson.* **1999**, *139*, 371–376.
56. Levitt, M. H.; Raleigh, D. P.; Creuzet, F.; Griffin, R. G. Theory and Simulations of Homonuclear Spin Pair Systems in Rotating Solids. *J. Chem. Phys.* **1990**, *92*, 6347–6364.
57. Madine, J.; Jack, E.; Stockley, P. G.; Radford, S. E.; Serpell, L. C.; Middleton, D. A. Structural Insights into the Polymorphism of Amyloid-like Fibrils Formed by Region 20−29 of Amylin Revealed by Solid-State NMR and X-ray Fibre Diffraction. *J. Am. Chem. Soc.* **2008**, *130*, 14990–15001.